Acta Crystallographica Section B
Structural Science
ISSN 0108-7681

A room-temperature X-ray diffuse scattering study of form (II) of the trimorphic molecular system *p*-(*N*-methylbenzylidene)-*p*-methylaniline

A. G. Beasley,[a] T. R. Welberry,[a]* D. J. Goossens[a,b] and A. P. Heerdegen[a]

[a]Research School of Chemistry, Australian National University, Canberra, ACT 0200, Australia, and [b]Department of Physics, Australian National University, Canberra, ACT 0200, Australia

Correspondence e-mail: welberry@rsc.anu.edu.au

Received 29 May 2008
Accepted 23 July 2008

Three-dimensional X-ray diffuse scattering data have been collected at room temperature for form (II) of the trimorphic molecular system *p*-(*N*-methylbenzylidene)-*p*-methylaniline. Although this polymorph has been reported to have a perfectly normal ordered average structure, strong and highly structured diffuse scattering was observed, indicating that substantial thermal disorder is present. A diffuse scattering analysis has been carried out using Monte Carlo simulation techniques. Narrow streaks of intensity extending between Bragg peaks in the $h0l$ section were found to arise from planes of diffuse scattering in three dimensions. These are caused by highly correlated molecular displacements along chains of end-to-end disposed molecules running in the $a-c$ direction, corresponding to methyl–methyl intermolecular interactions. A second significant feature – rods of diffuse scattering running in the b^* direction – indicates that molecular layers normal to b have a tendency to undergo lateral displacements with little correlation between layers. Finally, the internal flexibility of the molecule is required for a best fit. Changes in the two dihedral angles are found to be strongly correlated and show large excursions ($> \pm 20^\circ$) from the average values. All of these features suggest possible mechanisms for the way in which form (II) might transform to other polymorphs.

1. Introduction

Polymorphism refers to the situation where a substance crystallizes to give more than one crystal structure. In addition to its scientific interest, polymorphism is a matter of practical and commercial importance in the pharmaceutical industry and in the manufacture of pigments, dyes and explosives (Bernstein, 2002). In the pharmaceutical industry the polymorphic form of a compound can affect such things as ease of manufacture and processing, shelf-life, and, most importantly, the rate of uptake of the molecule by the human body. In extreme cases one crystal form at a particular dosage is effective and safe, while a second form at the same dosage is toxic (Knapman, 2000). There is clearly a great need to be able to understand, predict and control polymorphism.

Despite the attention that has been devoted to this problem, progress has been difficult and slow – a fact that may reflect the use of average (Bragg) crystal structures in the development of theoretical approaches. Efforts at crystal structure prediction, including the prediction of polymorphs, have had some success in the case of rigid molecules, but for conformationally flexible molecules – many pharmaceuticals are such molecules – success has been very limited (Lommerse *et al.*, 2000; Motherwell *et al.*, 2002; Day *et al.*, 2005). Despite the progress made, the goal of being able to predict a crystal structure (or crystal structures) of a molecule simply from a

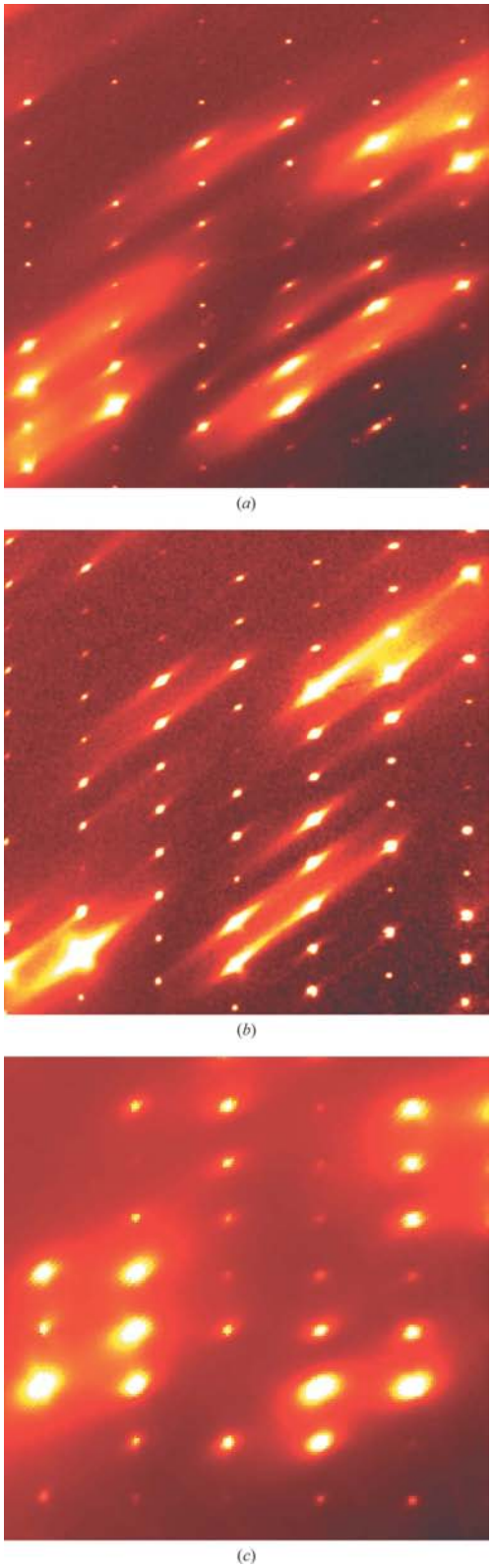

Figure 1
Small regions of the diffraction patterns of the three polymorphs of *p*-(*N*-methylbenzylidene)-*p*-methylaniline (MeMe), showing that all three contain strong highly structured diffuse scattering. (*a*) Region from the *h*0*l* section of polymorph (I); (*b*) region from the *h*0*l* section of polymorph (II); (*c*) region from the *h*0*l* section of polymorph (III).

Table 1
Cell data for the three polymorphs, (I), (II) and (III), of *p*-(*N*-methylbenzylidene)-*p*-methylaniline, $C_{15}H_{15}N$ (MeMe).

Polymorph	MeMe1 (I)	MeMe2 (II)	MeMe3 (III)
Space group	$P2_1/n$ (No. 14)	$P2_1$ (No.4)	$P2_1/c$ (No. 14)
a (Å)	6.0806 (1)	6.9016 (3)	9.8814 (3)
b (Å)	7.7537 (2)	7.1757 (5)	4.8848 (1)
c (Å)	26.0331 (7)	12.6325 (7)	12.0216 (3)
β (°)	90.131 (1)	102.643 (4)	90.493 (2)
V (Å^3)	1227.38	610.44	580.245
Z	4	2	2

structural formula is still a long way from being realized. The researchers involved have expressed the need for better energy models – that is, for more and better information about the forces between molecules. New theoretical approaches to this problem are continually being sought (Day *et al.*, 2007; Neumann *et al.*, 2008). In the latter work, for example, a specific force field was developed for each individual molecule to be studied.

A possible direct source of such information regarding the forces between molecules is the analysis of diffuse scattering, the weak continuous background of intensity found between the Bragg peaks in all diffraction patterns (see Fig. 1).

In conventional crystallography an analysis of Bragg peaks yields information about the average crystal structure of a compound. Diffuse scattering, by contrast, arises from the disorder in a crystal – any departure from the ideal of a perfectly periodic array of molecules – and since the disorder in a molecular crystal is conditioned by the forces between the molecules it follows that diffuse scattering contains information about intermolecular interactions. This includes, for example, information about how the motion of a molecule is correlated with the motion of its neighbours. Importantly, this is information that is unobtainable from Bragg peaks; Bragg peaks contain average one-body information only (*e.g.* atomic positions, site population parameters and mean-square amplitudes of displacement), while diffuse scattering contains two-body information.

The present study is part of a research program in which diffuse scattering methods are being applied to molecular crystal systems that exhibit polymorphism, with particular emphasis on systems containing molecules with conformational degrees of freedom. The title molecule, *p*-(*N*-methylbenzylidene)-*p*-methylaniline (henceforth MeMe), is a model example of polymorphic behaviour and was the subject of some early studies on polymorphism (Bernstein *et al.*, 1976; Bar & Bernstein, 1977, 1982). The system is trimorphic and all three polymorphs have been found to exhibit strong, highly structured diffuse scattering patterns (see Fig. 1). Cell data for the three polymorphs are given in Table 1. Of the three, form (II) is perhaps the most interesting since the *average* structure determination revealed it to be a perfectly normal ordered structure and yet it exhibits strong and highly structured diffuse scattering (see Fig. 1*b*), indicative of the presence of correlated molecular motions extending well beyond the unit-cell range. In this paper we describe in detail the analysis of the diffuse scattering for this form (II) polymorph (henceforth

MeMe2). The analysis of scattering for forms (I) and (III) will be the subject of future papers.

2. Experimental

2.1. Crystal growth

Single crystals of MeMe2 were obtained by evaporation of saturated ethanol solutions. MeMe2 appeared concomitantly with MeMe3. The crystal used in the room-temperature Bragg and diffuse scattering experiments was a colourless plate with dimensions 0.06 × 0.27 × 0.52 mm.

2.2. Bragg experiment

A previous crystallographic study of the MeMe system using room-temperature data found MeMe2 to be ordered (Bar & Bernstein, 1977), while MeMe1 and MeMe3 were disordered with two and four orientations of the molecule, respectively, on a given molecular site of the average structure (Bar & Bernstein, 1982; Bernstein *et al.*, 1976). This previous study of MeMe2 obtained a low residual factor of $R = (\sum |F_{obs} - F_{calc}|)/(\sum |F_{obs}|) = 0.046$ and found no evidence of structural disorder. However, for the present work, to confirm these early findings and to obtain more accurate unit-cell parameters, the average crystal structure of MeMe2 was redetermined (at 294 K). The cell data obtained are given in Table 1, where they are compared with those for forms (I) and (III) (Beasley *et al.*, 2008). The residual factor obtained was $R = 0.043$ for 1192 reflections for which $I_{obs} > \sigma$. Fig. 2 shows a plot of one molecular layer in the average structure. A second molecular layer, related to that shown by a 2_1-screw axis at the origin of the unit cell, has been omitted for clarity.

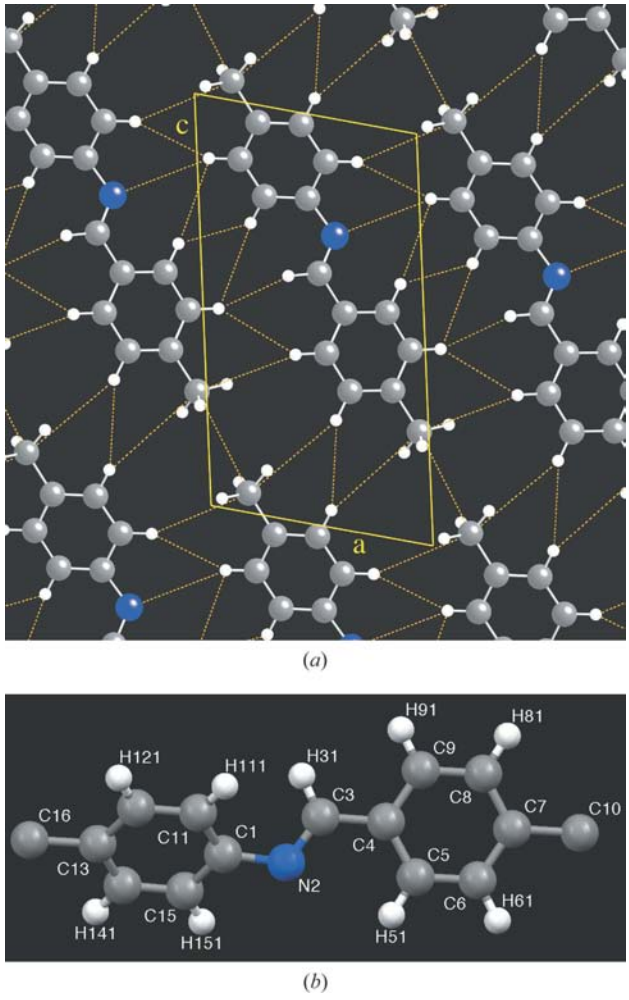

Figure 2
(*a*) Drawing of a single molecular layer of the average structure of MeMe2 viewed down [010]. The second molecular layer (omitted for clarity) is related to that shown by a 2_1 screw axis at the origin of the unit cell. The intermolecular vectors shown as dashed lines correspond to the vectors used in the diffuse scattering analysis (see later). (*b*) Drawing of the molecule showing the atomic labelling. Note that the methyl H atoms have been omitted. See also Table 3.

2.3. Diffuse scattering experiment

Three-dimensional X-ray diffuse scattering data were collected at room temperature on the 1-ID-C beamline at the Advanced Photon Source synchrotron. The photon energy was 40 keV [$\lambda = 0.30997\,(1)$ Å]. Frames of data were collected using a Mar345 image-plate area detector with a pixel resolution of 0.15 mm. A detector diameter of 300 mm was used, giving frames of size 2000 × 2000 pixels. The sample-to-detector distance was determined using a CeO_2 powder standard as 292.658 mm. The crystal was exposed for 10 s for each frame and was simultaneously rotated through 0.36°. 508 such frames were collected, giving 182.88° of angular coverage. Reciprocal-space sections were reconstructed from the frames using the programs *XDS* (Kabsch, 1993) for indexing of Bragg peaks and *XCAVATE* (Estermann & Steurer, 1998) for reconstruction of specified two-dimensional reciprocal sections. Data from symmetry-related regions were merged. This gave data out to a maximum $\sin\theta/\lambda$ of approximately 0.76 Å^{-1}.

2.4. Processing of diffuse scattering data

The recording of diffuse scattering data as described above is still a far from routine process, and numerous problems are encountered that would have negligible impact on a Bragg experiment but are of great importance for diffuse scattering. Some of the problems encountered are ubiquitous in these kinds of experiment and have been described previously (Welberry *et al.*, 2005). In the present case, the raw frames of data included air scattering, as well as two different kinds of artefact (see below). In addition, individual frames varied in scale as a result of variations of exposure caused by shutter synchronization problems and of variations in the amount of sample in the beam at different angles of rotation. To correct for air scattering, a blank (background) was subtracted from each frame. To correct for differences in intensity of different frames, the median intensity of each frame was used as a scale. The first of the two types of artefact (which resulted in radial streaking in reconstructed images) was due to blooming caused by the backscattering of Bragg peaks from the metal mounting spindle at the rear of the detector. The second type

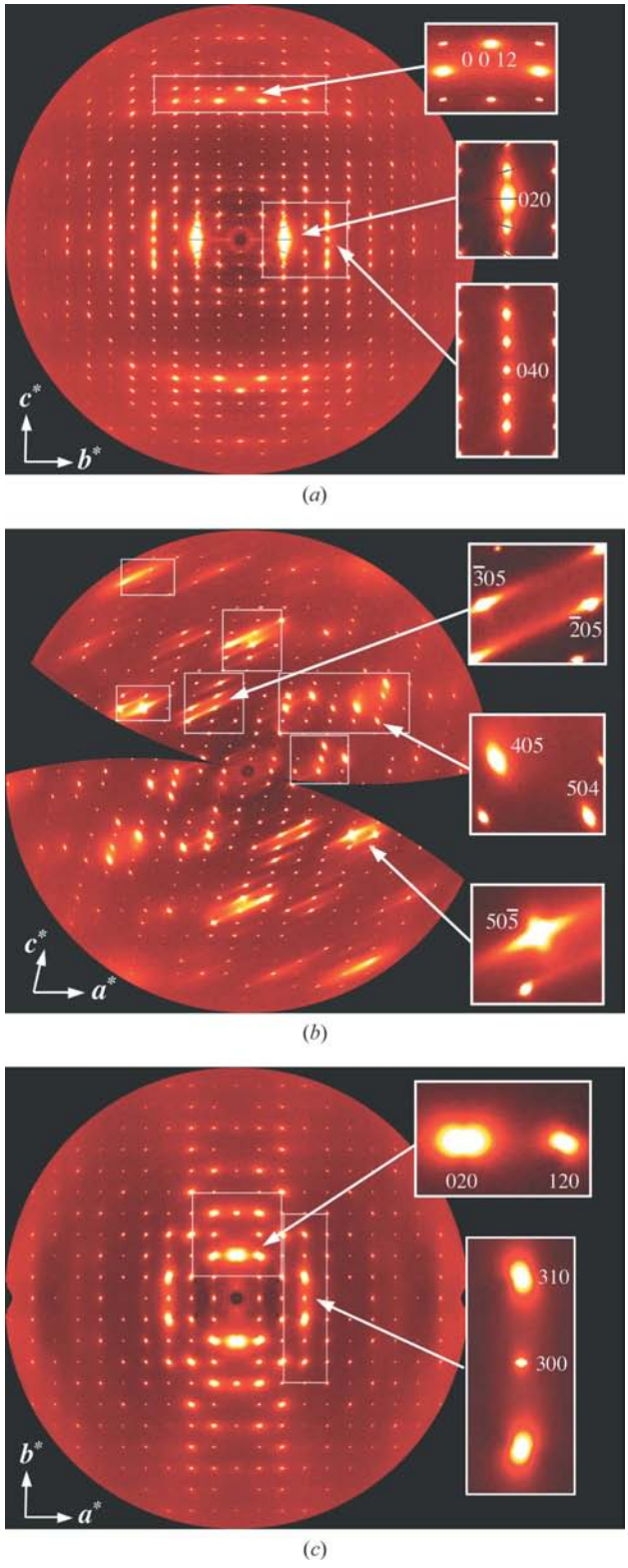

Figure 3
Three basal sections of the observed diffuse scattering in form (II) of *p*-(*N*-methylbenzylidene)-*p*-methylaniline. (*a*) 0*kl*; (*b*) *h*0*l*; (*c*) *hk*0. The superimposed white rectangles indicate the ten regions of data used in the fitting. Inset are enlarged small regions of the pattern that are referred to in the text. Some of these are on a reduced intensity scale in order to show the detail.

of artefact (arc-shaped streaks on the raw data frames) was due to an electronic fault in the detector during readout. The artefacts were removed by software that located and masked affected pixels in the frames. This resulted in some loss of data. Affected pixels appear black in the images of the data shown in Fig. 3 and were ignored during the analysis.

2.5. Observed diffuse scattering data

Fig. 3 shows the three basal planes of reciprocal space. Structured diffuse scattering is present as elongated diffuse peaks at Bragg peak positions and as diffuse streaks extending between Bragg peaks. The *h*0*l* section is particularly rich in detail. Some of the most significant features in each section are shown (inset) as enlargements. We summarize these features as follows:

2.5.1. *0kl* section. The strongest diffuse peak is associated with the Bragg peak at 020, with two smaller peaks immediately above and below it at 021 and $02\bar{1}$ (Fig. 3*a*). Close inspection reveals the latter two peaks to be very slightly tilted away from the vertical. There is also a column of peaks at 04*l* ($l = 0, \pm1, \pm2$) with weak bands of intensity extending between the $l = 1, 2$ peaks and the $l = -1, -2$ peaks. In addition, this section has a distinctive group of three peaks at 00,12, 01,11 and $0\bar{1}$,11, with the latter two being slightly tilted away from the horizontal.

2.5.2. *h0l* section. The most striking feature is the set of narrow streaks of intensity extending diagonally in the $a^* + c^*$ direction (*e.g.* near $\bar{3}05$ and $\bar{2}05$) (Fig. 3*b*). It should be noted that these streaks may also be seen in non-integral sections of the three-dimensional data, such as *hkl* (k = 0.1, 0.2, 0.3, 0.4, 0.5), as well as in other integral sections ($k = 1, 2, 3$). Consequently, these streaks are in fact diffuse planes of scattering rather than diffuse *rods*. There are also a number of peaks (*e.g.* 405) that are elongated in a direction perpendicular to the diagonal streaks. Around the $50\bar{5}$ position both the streaks and the perpendicular elongated peaks are present simultaneously.

2.5.3. *hk0* section. The strong 020 peak is again visible in this section (Fig. 3*c*). Here it has a dumbell appearance with a distinct narrowing around the middle. The nearby 120 peak is similar in shape but is inclined to the horizontal so that it is perpendicular to a radial vector from the origin.

3. Diffuse scattering analysis

Monte Carlo (MC) computer simulation of a model structure has become a powerful and well accepted technique for aiding the interpretation and analysis of diffuse scattering patterns (Welberry, 2004; Weber *et al.*, 2001; Weber & Bürgi, 2002). In this method a computer model is set up based on known physical and chemical principles with adjustable parameters describing the basic interatomic or inter- and intramolecular interactions and possible mechanisms for disorder. Diffraction patterns are then calculated from the results of the simulations and these are compared with the observed data. As a result of the comparison adjustments are made to the model para-

Table 2
The *z*-matrix used to represent the MeMe molecule.

Entries *i*, *j* and *k* refer to atom numbers and specify the connectivity of the molecule. Atoms *x*1 and *x*2 are dummy atoms. Atoms C5 and C11 were used to control the conformation of the molecule. The two dihedral angles, L_1 and L_2, that were allowed to vary have been printed in bold and marked with asterisks.

Atom number	Atom label	*i*	Bond length (°)	*j*	Bond angle (°)	*k*	Dihedral angle (°)
1	*x*1	0	0.000	0	0.00	0	0.00
2	*x*2	1	0.500	0	0.00	0	0.00
3	C3	1	0.632	2	118.55	0	0.00
4	H31	3	1.000	1	118.54	2	179.92
5	C4	3	1.455	4	118.75	1	−179.95
6	C5	5	1.393	3	122.24	4	**177.13***
7	H51	6	0.999	5	119.48	3	−1.29
8	C6	6	1.379	7	119.60	5	−179.76
9	H61	8	0.999	6	119.30	7	0.03
10	C7	8	1.378	9	119.34	6	179.82
11	C10	10	1.512	8	120.94	9	2.82
12	C8	10	1.385	11	121.02	8	−178.47
13	H81	12	0.999	10	119.37	11	−2.95
14	C9	12	1.388	13	119.60	10	−179.83
15	H91	14	0.999	12	119.54	5	179.71
16	N2	3	1.265	5	122.69	4	−179.92
17	C1	16	1.421	3	119.32	5	178.06
18	C11	17	1.384	16	123.28	3	**−42.26***
19	H111	18	0.999	17	119.71	16	1.95
20	C12	18	1.382	19	119.57	17	179.87
21	H121	20	1.000	18	119.51	19	−0.11
22	C13	20	1.383	21	119.44	18	−179.76
23	C16	22	1.512	20	121.56	21	−1.47
24	C14	22	1.380	23	120.28	20	177.66
25	H141	24	0.999	22	119.49	23	1.94
26	C15	24	1.384	25	119.46	22	−179.89
27	H151	26	0.999	24	119.60	17	179.50

meters, and the process is repeated until agreement between observed and calculated patterns is obtained.

The aim of the present study was to develop an MC model that is able to reproduce the observed diffraction patterns in as detailed and quantitative manner as possible, with particular attention paid to the characteristic diffraction features highlighted in Fig. 3. Since the MeMe2 polymorph is found to have an ordered average structure it was assumed from the outset that the disorder giving rise to the diffuse scattering is purely thermal in origin. To this end the analysis involved, in outline, the following steps:

3.1. Average structure

An accurate average crystal structure for MeMe2, a $Z = 2$ structure, was first obtained. Details of this determination will be reported elsewhere.

3.2. Monte Carlo model

An MC computer model was constructed using the atomic coordinates derived from the average structure determination. First a *z*-matix description of these coordinates was derived so that the whole structure could be defined by the contents of the *z*-matrix, two quaternions defining the molecular orientations and two sets of translations defining their positions in the unit cell. The *z*-matrix used in the analysis is given in Table 2. Molecules were treated as a number of rigid fragments with only the rotations around single bonds providing internal flexibility. The two dihedral angles that were allowed to vary have been marked with asterisks. All other entries in the *z*-matrix were kept constant throughout.

During the simulation the two dihedral angles were allowed to vary but deviations away from the values observed in the average structure invoked an energy penalty. This was modelled using torsional Hooke's law springs [see equation (1) below]. Similarly the positions and orientations of the whole molecules were allowed to vary and deviations away from the average structure invoked an energy penalty, which was modelled using sets of linear Hooke's law (harmonic) springs connecting neighbouring molecules. These springs were placed along a carefully selected subset of the large number of atom–atom vectors that typically make up a given intermolecular interaction. This subset of atom–atom interactions constitute the *effective* intermolecular interactions that are used in the simulations. Use of such effective interactions is necessary to reduce the computational task to a tractable level. In choosing these vectors the aim was to reduce the number to a manageable level while retaining a sufficient number to define robustly the separation and mutual orientation of neighbouring molecular fragments. For each pair of neighbouring molecular fragments two or three such atom–atom vectors are usually sufficient. Provided these define the separation and mutual orientation of the fragments, the actual choice of vector is unimportant. The selection of vectors is a sufficiently flexible process that additional vectors can be added or redundant ones removed quite easily at any stage, should the initial selection prove to be deficient. Table 3 lists the vectors that were used in the analysis. Fig. 2 shows those vectors linking molecules within one molecular plane. In all, 39 unique types of vector were used, each of these requiring the specification of a unique spring constant, K_i. Together with two torsional spring constants, L_i, the total number of parameters determined in the analysis was 41. Each molecule in the crystal is surrounded by 14 neighbours which occur in seven symmetry-related pairs.

3.3. Simulation

Initial values were assigned to the K_i and L_i force constants, and then MC simulation was carried out on the model crystal. The majority of the simulations were carried out using a model crystal comprising $32 \times 32 \times 32$ unit cells. In later stages of the analysis this was increased to $48 \times 48 \times 48$ unit cells to allow better quality diffraction patterns to be computed. The model crystal was initially set up by placing copies of the molecule in each cell using the *z*-matrix, quaternions and translation vectors. Rather than commencing the simulation with a perfect crystal of identical molecules, some uncorrelated disorder was introduced by perturbing randomly the positions, orientations and conformations of all molecules away from their observed average values. The MC energy used in the simulation was of the form

Table 3
Summary of the interaction vectors used.

Examples given here are for the molecule with symmetry x, y, z. N = neighbour identifier; V = vector type; O = origin atom; C = cell translation of destination molecule with respect to origin molecule; S = symmetry relationship of destination molecule to origin molecule; D = destination atom; L = length of vector; $F1$ = spring constant, K_i (qualitative); $F2$ = spring constant, K_i (quantitative); L_1 and L_2 are the torsional force constants.

N	V	O	C	S	D	L	$F1$	$F2$
1	1	C8	000	*A*	H111	3.038	0.125	1.319
	2	C5	000	*A*	H91	3.082	0.125	–
	3	H31	000	*A*	C6	3.258	0.125	–
	4	H31	000	*A*	C7	3.265	0.125	1.083
	5	H31	000	*A*	C8	3.299	0.125	2.005
	6	C3	000	*A*	C9	3.570	0.125	1.353
	7	C10	000	*A*	C12	3.617	1.250	2.087
	8	C10	000	*A*	H111	3.690	1.250	2.701
	9	C10	000	*A*	C13	3.955	1.250	1.892
	10	C8	000	*A*	C15	4.224	0.125	0.149
2	11	H51	$\bar{1}00$	*B*	H111	2.299	0.125	1.844
	12	H51	$\bar{1}00$	*B*	H121	2.795	0.125	0.186
	13	H31	$\bar{1}00$	*B*	H61	2.832	0.125	2.746
	14	H61	$\bar{1}00$	*B*	H111	2.834	0.125	–
	15	H121	$\bar{1}00$	*B*	H151	2.880	0.125	–
	16	C2	$\bar{1}00$	*B*	H121	3.169	0.125	2.788
	17	H61	$\bar{1}00$	*B*	H91	3.216	0.125	0.461
	18	C16	$\bar{1}00$	*B*	H151	3.224	1.250	2.034
	19	C10	$\bar{1}00$	*B*	H91	3.403	1.250	0.719
3	20	H81	$00\bar{1}$	*C*	H141	2.958	0.125	0.077
	21	H81	$00\bar{1}$	*C*	C16	3.509	1.250	0.671
	22	C10	$00\bar{1}$	*C*	H141	4.059	1.250	1.284
4	23	C10	$10\bar{1}$	*D*	C16	3.691	6.250	6.376
5	24	C5	100	*E*	H61	3.185	0.125	0.629
	25	C4	100	*E*	H61	3.265	0.125	0.094
	26	H61	100	*E*	C9	3.442	0.125	–
	27	H51	100	*E*	C10	3.599	1.250	0.885
	28	C10	100	*E*	H151	4.020	1.250	–
	29	C10	100	*E*	C2	4.274	1.250	1.123
	30	C5	100	*E*	C10	4.321	1.250	1.745
	31	C4	100	*E*	C10	4.522	1.250	–
6	32	C12	001	*F*	H141	2.893	0.125	–
	33	C13	001	*F*	H141	2.997	0.125	2.803
	34	C14	001	*F*	H141	3.164	0.125	0.732
	35	C16	001	*F*	H151	3.372	1.250	2.199
	36	C16	001	*F*	C15	3.991	1.250	0.876
	37	C2	001	*F*	C16	4.162	1.250	1.109
7	38	H121	$\bar{1}01$	*G*	C16	3.371	1.250	2.232
	39	C16	$\bar{1}01$	*G*	C16	4.334	1.250	0.869
L_1							10.0	12.13
L_2							10.0	10.96

Symmetry codes: (*A*) $1-x, \frac{1}{2}+y, 1-z$; (*B*) $-1+x, y, z$; (*C*) $x, y, -1+z$; (*D*) $1+x, y, -1+z$; (*E*) $2-x, \frac{1}{2}+y, 1-z$; (*F*) $1-x, \frac{1}{2}+y, 2-z$; (*G*) $-x, \frac{1}{2}+y, 2-z$.

$$E = \sum_{\substack{\text{all linear}\\ \text{springs}}} K_i(d-d_0)^2 + \sum_{\substack{\text{torsional}\\ \text{springs}}} L_i(\varphi-\varphi_0)^2. \qquad (1)$$

Here d and φ are instantaneous values of the spring lengths and torsion angles, respectively, and d_0 and φ_0 are the corresponding mean values obtained from the average structure. A sufficient number of MC cycles were performed for the system to attain (or closely approach) equilibrium. 2500 MC cycles were used initially, but in later stages of the analysis this was increased to 10 000. One MC cycle is defined as that number of individual MC steps required to visit each molecule once on average. The force constants K_i and L_i are scaled relative to k_BT, where k_B is Boltzmann's constant. Hence, in the simulations k_BT has a value of unity irrespective of the energy units chosen.

3.4. Data used for the refinement

It is still far from being computationally feasible to carry out analyses using complete three-dimensional diffuse scattering data. In these circumstances two different approaches have been tried. In the first, data for a small number of complete reciprocal sections (perhaps three or four) have been used (Welberry & Heerdegen, 2003; Welberry *et al.*, 2001). As an alternative to this a second approach has been to use a number of selected areas which include the strongest and most structured diffuse scattering features (Welberry *et al.*, 1998). In the latter case it is supposed that these regions of strong intensity contain the most important information. The added advantages of this latter approach are that data at a higher spatial resolution can be employed for these smaller regions and valuable computation time is not spent calculating large areas of very weak or zero scattering. It is this second approach that has been used in the present case.

For the present analysis data from ten separate areas taken from the three reciprocal sections shown in Fig. 3 were used. These regions are indicated by the white outlined rectangular boxes. They were chosen to include the strong features shown as enlarged insets in Fig. 3 but also to include a complete range of intensity from very weak areas to the strongest features and to include a wide range of $\mathbf{Q}$ ($= 4\pi\sin\theta/\lambda$). Clearly, once a model has been derived, complete reciprocal lattice sections can be computed for comparison with the observed patterns as a crosscheck.

3.5. Qualitative fitting

The suitability of the initial springs and force constants was then tested by calculating reciprocal-space sections from the atomic coordinates produced by the simulation and comparing these, qualitatively, with observed sections. The springs and force constants were then adjusted (manually) as a result of this comparison. The adjustments made were aimed at increasing (or decreasing) correlations in particular directions. If it appeared that extra correlation was required in a direction that the current set of springs was unable to provide then further springs could be added during this stage. The whole process of simulation followed by diffuse calculation and comparison with observation was repeated over a number of cycles until satisfactory qualitative agreement between observed and calculated sections was achieved.

This qualitative fitting stage of the analysis can be viewed as one of experimentation with the model to see that the basic criteria for the interactions discussed in §3.2 are satisfied and the model is capable of reproducing the observed diffraction

features. For the present model this process was relatively straightforward, but for a system involving occupational disorder as well as thermal disorder and possible size-effect relaxations it can be much more involved (see *e.g.* Goossens *et al.*, 2008).

3.6. Final quantitative refinement

A final quantitative automatic least-squares refinement was carried out using the procedure described by Welberry *et al.* (1998) to produce an improved set of force constants from the best set obtained from the qualitative fitting. In this method the system parameters – in this case K_i and L_i [see equation (1)] – are then iteratively adjusted until the best agreement is obtained between the observed diffraction patterns and those calculated from the model coordinates. At each stage of the refinement, a goodness-of-fit parameter χ^2 is used as a quantitative measure of the agreement of the model diffraction pattern with the observed data

$$\chi^2 = \sum_{h,k,l,m} \omega_{hklm} (\Delta I)^2, \tag{2}$$

where

$$\Delta I = I_{\rm obs} - (b_m + f_m I_{\rm calc}). \tag{3}$$

Here, the summation is over all non-integral reciprocal points h, k, l corresponding to individual pixels in the m measured sections of data. f_m is a scale and b_m a background correction applied to section m. [Note that b_m and f_m are determined as described by Proffen & Welberry (1997) and are not included as variables in the least-squares matrix]. ω_{hklm} is the weight for the corresponding data point h, k, l of data plane m. The weights used in the work described here were taken as $\omega_{hklm} = 1/I_{\rm obs}$. Numerical estimates of the differentials of χ^2 with respect to the model parameters are calculated by performing additional simulations in which each parameter in turn has been incremented by a small amount δ. These differentials are then used to form the least-squares matrix and provide automatic updating of the parameters before the next iteration.

The final set of force constants produced by the refinement is given in Table 3. Comparison of the starting and final values reveals that in some instances a parameter was refined to a value of zero, the result being to reduce the number of model parameters from 41 to 33. A simulation using this final set of springs and force constants was carried out, and the resulting model structure was then available for further interrogation and analysis.

4. Results

As a confirmation that the final structure resulting from the MC simulation is consistent with the average structure determined from the Bragg experiment, we show in Fig. 4 a plot of the atomic (non-hydrogen) positions for one molecular site from all $48 \times 48 \times 48$ unit cells in the simulated structure superposed in a single unit cell. This is shown alongside a plot of the displacement ellipsoids obtained from the average structure refinement. There is generally very good correspondence, with only the methyl groups displaying a moderate degree of anisotropy.

4.1. Calculated diffraction patterns

Fig. 5 shows calculated diffraction patterns for three reciprocal sections corresponding to those for the observed data shown in Fig. 3. The insets show as enlargements the distinctive scattering features that were also highlighted in the observed data. There is clearly very good agreement between the observed and calculated patterns. This is reflected in the agreement factor that was obtained for the final model. After four cycles of refinement, $wR_2 = [\sum \omega(\Delta I)^2 / \sum \omega I_{\rm obs}^2]^{1/2}$ was 0.220, for an $\omega = 1/I_{\rm obs}$ weighting scheme on a pixel-by-pixel comparison over the ten selected regions which comprised in total 27 722 pixel data points. As compared with unit weights, an $\omega = 1/I_{\rm obs}$ weighting scheme is more sensitive to the intensity between Bragg peaks but is more vulnerable to noise. Both weighting schemes were tested, with broadly similar results.

Of the 33 non-zero refined force constants, K_i, given in Table 3, that along the vector 23, which links the methyl group of one molecule with that on the next molecule in a chain running in the $a-c$ direction, is by far the largest. It is this interaction that is responsible for producing the narrow diffuse streaks in the neighbourhood of the $\bar{3}05$ and $\bar{2}05$ reflections (and in other regions) highlighted in Fig. 1. To demonstrate the effect of this single spring, Fig. 6 shows an enlarged region of the $h0l$ section calculated for the final

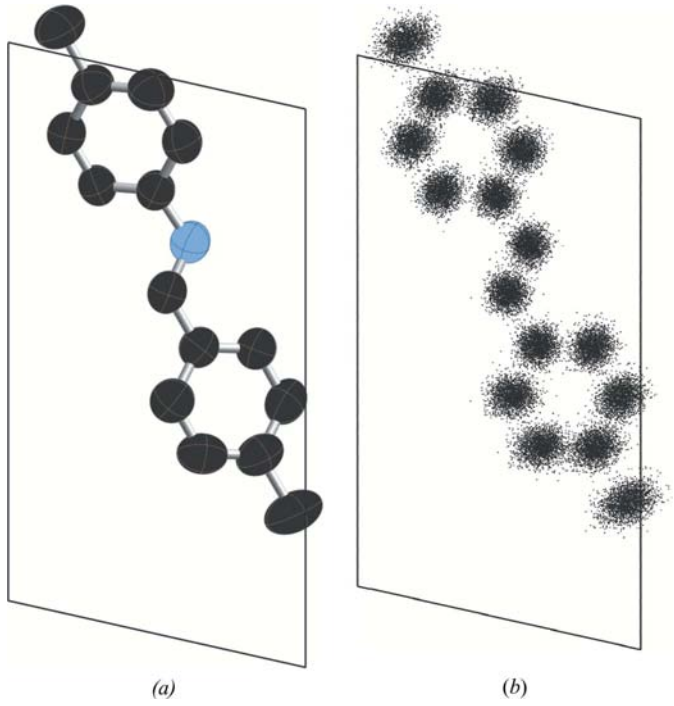

Figure 4
Plots of (*a*) the anisotropic displacement ellipsoids (66% probability level) compared with (*b*) the scatterplot of atomic positions for a single molecular site in the final MC simulation.

model (Fig. 6*a*) in comparison with the same region calculated from a model in which this force constant has been set to zero, with all others remaining unchanged (Fig. 6*b*). Removing this single spring has little effect on other features in the diffraction patterns and the overall agreement factor for the whole 27 722 data points used in the refinement is only raised by 1.7%. Fig. 6(*c*) shows the same region for the $h\frac{1}{2}l$ section as for the *h*0*l* section in Fig. 6(*a*), showing how the streaks are in fact *planes* of scattering.

Figs. 6(*d*) and 6(*e*) show comparative plots of an enlarged region of the *hk*0 section for the final model and a model in which the spring constants within a molecular layer normal to *b* have been increased by a factor of 3. Fig. 6(*f*) shows a drawing of the structure in projection down *c* showing these molecular layers. Increasing these spring constants has the effect of making the (vertical) diffuse rod of scattering that links the $3\bar{2}0$, $3\bar{1}0$, 300, 310 and 320 reflections more distinct and decreases the background scattering between the columns of Bragg peaks. This rod of scattering is indicative of the fact that these molecular layers tend to move in concert laterally in directions normal to *b* and the motion in one layer is to a large extent not correlated with that of the next. The fitted model (Fig. 6*d*) indicates that this effect is occurring but not as markedly as in the modified model (Fig. 6*e*).

4.2. Displacement correlations

A useful way of interrogating the final model coordinates, in order to gain an appreciation of how the molecules are behaving, is to display the way in which the displacements of neighbouring molecules (or parts thereof) are correlated with each other. This can be achieved by plotting so-called peanut diagrams. If X_A is the component of the displacement of molecule *A* in a direction defined by an angle φ from some reference direction and X_B is the component of the displacement of molecule *B* in the same direction then the correlation coefficient, C_φ, for these displacements is given by

$$C_\varphi = \langle X_A X_B \rangle / \left(\langle X_A^2 \rangle \langle X_B^2 \rangle \right)^{1/2}. \qquad (4)$$

Fig. 7 shows plots of C_φ for displacements of the centre of mass of two types of neighbouring molecule. Inset in each figure is a drawing of the molecular pair involved. $\phi = 0$ corresponds to a displacement direction parallel to *c*. The peanut-shaped locus gives the value of the correlation coefficient for displacements in a given direction. Fig. 7(*a*) indicates that for molecules interacting *via* the Me···Me contact (vector 23 in Table 3) there is strong correlation between the displacements directed along the length of the molecule and much weaker correlation between their lateral displacements. It is this correlated motion that gives rise to the characteristic streaks seen in Fig. 6(*a*). Since this correlation acts along a one-dimensional chain of molecules the diffuse streaks are, in fact, planes of scattering in three dimensions and may be observed in non-integral layers normal to *b* as shown in Fig. 6(*c*).

Fig. 7(*b*) shows the same kind of plot for the pair of molecules separated by a cell translation along *a*. Note that this has an even larger correlation value than that for the

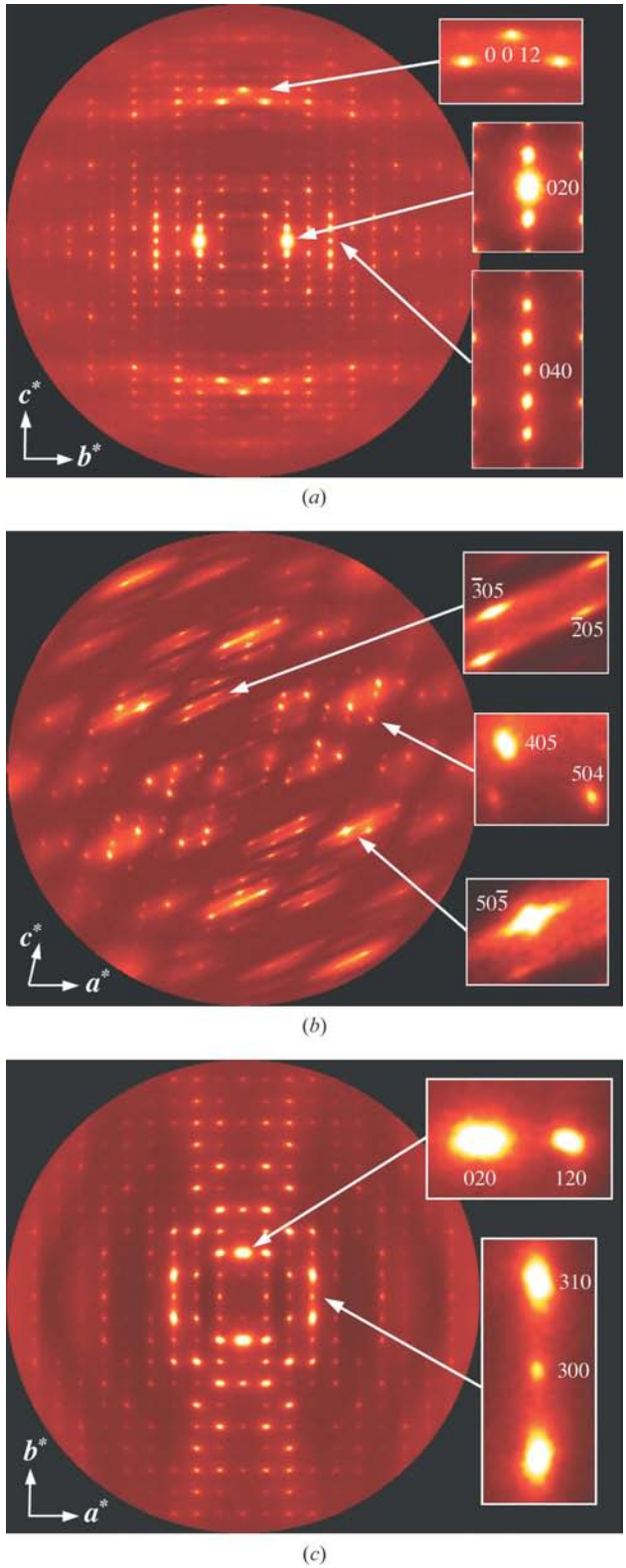

Figure 5
Three basal sections of diffuse scattering calculated from the final Monte Carlo simulation. (*a*) 0*kl*; (*b*) *h*0*l*; (*c*) *hk*0. Inset are enlarged small regions of the pattern that are referred to in the text. Some of these are on a reduced intensity scale in order to show the detail. Note that these plots are of the *diffuse* scattering only; the average structure, which gives rise to the Bragg peaks, has been subtracted.

Me···Me contact shown in Fig. 7(*a*), but since the *a* cell repeat is much smaller than the length of the molecule this correlation decays more rapidly with distance and does not lead to features as sharp as the diffuse streaks due to the Me···Me contact. It does, however, contribute to the diffuse band of scattering discussed above in relation to Figs. 6(*d*) and 6(*e*). The minimum value for C_φ corresponds to a direction along the length of the molecules, indicating that they can easily slide relative to each other in that direction. It is also seen that the direction of maximum correlation is not directly along *a* but reflects the fact that the top of one molecule interacts most strongly with the bottom of the neighbouring molecule.

4.3. Torsional force constants

Another point of interest in the present study was whether the analysis was sensitive to the intramolecular torsional force constants. The refined values for the two force constants L_1 and L_2 are given in Table 3. These values are similar to the torsional force constant determined in an earlier study for benzil (Welberry *et al.*, 2001; 0.159 deg^{-1} = 9.11 rad^{-1}). To test the importance of the force constants a simulation was carried out for a model that used the final set of the linear spring force constants but with completely rigid molecules. This resulted in an increase in the agreement factor, *R*, of slightly more than 1%. In the earlier study of benzil, inclusion of the intramolecular torsional force constants made 4% difference in the final *R*. It thus appears that, although the flexibility of the molecule contributes significantly to the fit obtained, it is relatively less important for the present system than in the benzil system.

Fig. 8 shows a scatter diagram of the two torsion angles L_1 and L_2 that are present in the final model realization. If the two angles were completely uncorrelated then this plot would be circularly symmetric. The marked anisotropy clearly shows that the deviations of the two angles away from their mean position are strongly correlated (correlation coefficient −0.41). The negative value means that the correlated motion tends to maintain the relative orientation of the two rings that is found in the average conformation. It should be noted that the molecule is nonplanar.

5. Conclusion

In this paper we have described a simple MC model that reproduces in detail the diffuse diffraction patterns that have been observed for MeMe2 [form (II) of *p*-(*N*-methylbenzylidene)-*p*-methylaniline]. A quantitative fit with final agreement factor $R = [\sum \omega(\Delta I)^2 / \sum \omega I_{\rm obs}^2]^{1/2} = 0.220$ was obtained for 27 722 data points constituting ten selected two-dimensional regions of the three-dimensional diffraction patterns. These regions contained representative examples of the strong and highly structured diffuse scattering that is observed, as well as regions of low intensity. Qualitative comparisons over numerous complete reciprocal lattice sections have confirmed that the MC model provides a very good description of the full three-dimensional scattering.

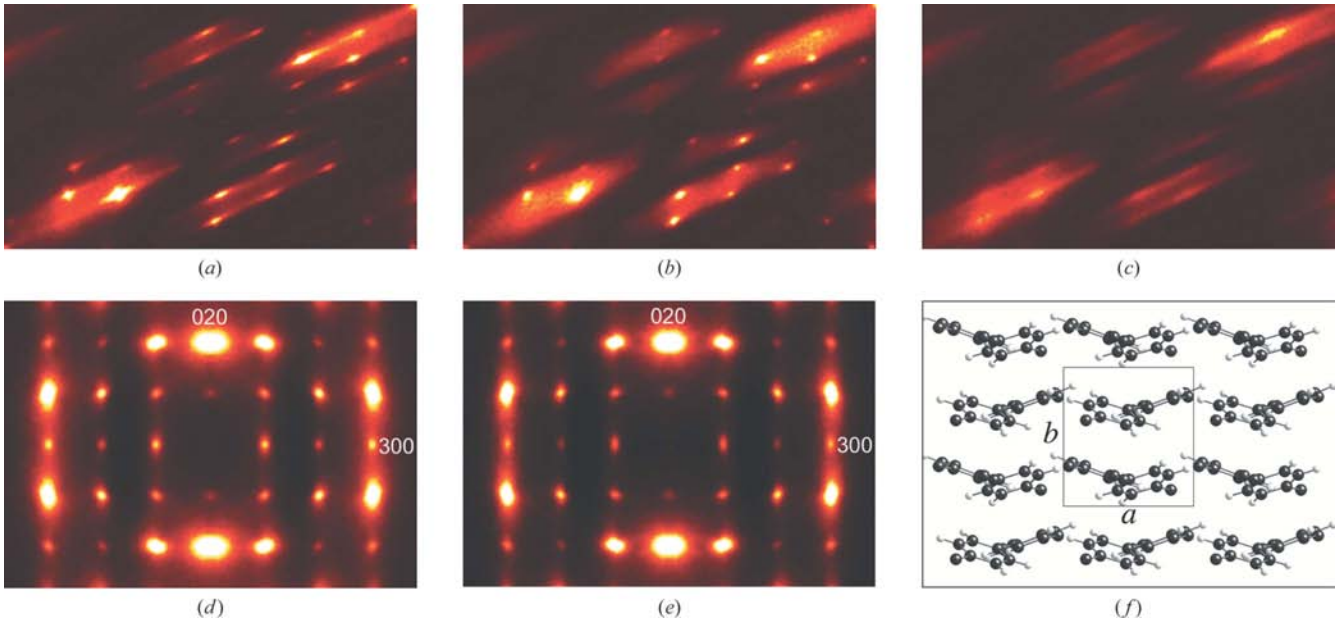

Figure 6
(*a*) Region of the *h*0*l* section calculated using the final set of spring force constants. (*b*) The same region as in (*a*) calculated using the same model but with the Me···Me force constant (vector 23 in Table 3) set to zero. (*c*) Region of the $h\frac{1}{2}l$ section of the same model as (*a*) and for the same range of *h* and *l*. (*d*) Region of the *hk*0 section calculated using the final set of spring force constants. (*e*) The same region as in (*d*) calculated using a model with the force constants for neighbour types 2 and 5 in Table 3 increased by a factor of 3. (*f*) Projection of the structure down *c* showing the molecular layers normal to *b*. Note that all of the diffraction patterns are of the *diffuse* scattering only; the average structure, which gives rise to the Bragg peaks, has been subtracted.

The model is purely thermal in nature, confirming the results from Bragg scattering that this polymorph is indeed a perfectly normal ordered molecular system. The model uses effective interactions in the form of 33 different types of harmonic (Hooke's law) springs to represent the intermolecular forces and two harmonic torsion springs on the two internal dihedral angles which give the molecule flexibility.

It should be emphasized that the derivation of this set of spring constants which make up the effective interactions should not be regarded as a rigorous attempt to reproduce in fine detail the forces and energies between molecules. Rather they should be regarded as purely a means to an end – the production of a model that fits the experimental data and that approximates the behaviour of the real crystal system. The aim in obtaining such a model is not to attempt to provide more detailed information regarding the intermolecular potentials, such as those used in efforts at crystal structure prediction described in §1, but to provide additional observational data with which to inform the development of those more rigorously conceived potentials that to date have relied solely on the observation of average Bragg structures.

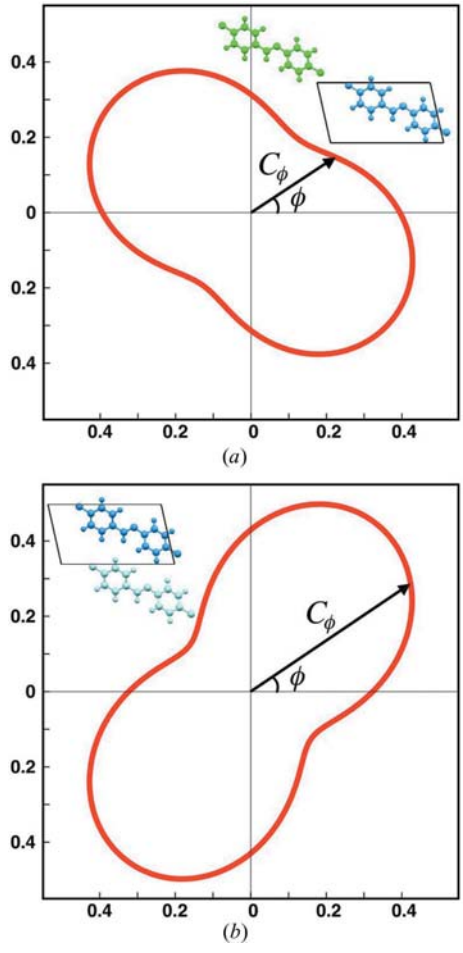

Figure 7
Plots of the displacement correlation function C_φ (peanut diagrams) for the displacements of the centre of mass of two different neighbouring pairs of molecules.

The most significant result of the analysis is that the spring along the vector 23 in Table 3, which links the methyl group of one molecule with that on the next molecule along $a-c$, was found to have by far the largest spring constant. It has been shown that this leads directly to the strong and very characteristic diffuse streaking that is observed in the diffraction patterns. This single interaction induces strong longitudinal displacement correlation along single chains of molecules running in the $a-c$ direction. It was further found that removal of this spring has little effect on the rest of the diffraction pattern, indicating that this motion is close to being an eigenstate of the system. As such it may be considered to be akin to a soft mode of vibration and indicative of the fact that the system is in a shallow energy minimum. It might be conjectured that this could facilitate the transformation to a different polymorphic state.

A second feature of the analysis that has been highlighted in §4.2 is the presence of rods of diffuse scattering running in the b direction (shown in Figs. 6*d* and 6*e*). This feature arises from the concerted motion of molecular layers normal to b sliding laterally more or less independently of each other. This effect is not nearly as pronounced as the correlated chains of molecules described above, but it does suggest an additional mechanism by which change to a different polymorph might occur.

Finally, the analysis has revealed information regarding the flexibility of internal torsion angles. Though, compared with a recent study of benzil, the contribution to the overall agreement factor was relatively small, there was a clear indication that molecular flexibility needs to be taken into account to obtain the best fit to the data. The determined values for the torsional force constants were of a similar magnitude to those found for benzil, but perhaps more importantly it was found that the magnitudes of the variation of the dihedral angles was quite large. It may be seen from Fig. 8 that excursions away from the average position for each dihedral angle frequently exceeded 0.4 radians or 23°. Since it is thought that polymorph

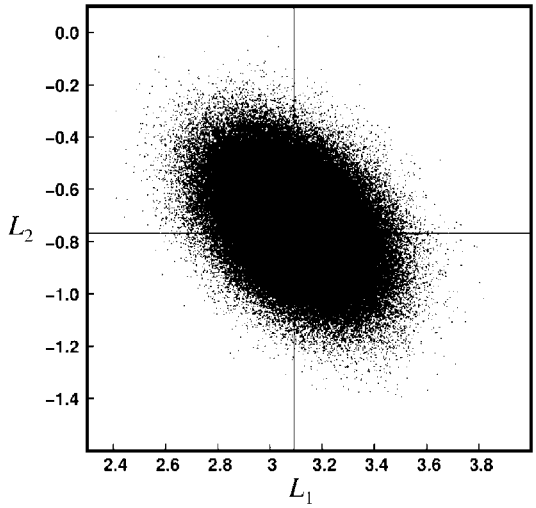

Figure 8
Scatterplot of the distribution of the two torsional angles L_1 and L_2 (in radians) over all molecules in the final model realization.

(III) of MeMe has dynamic disorder of the —C═N— bridge, the large-amplitude (but correlated) excursions observed here could be considered to be precursors of that effect too.

Analyses of the other two (disordered) polymorphs of MeMe as well as temperature-dependent studies of the diffuse scattering are still in progress, and it will be interesting, when results for these are available, to see whether the relationship between the different polymorphs can be understood in terms of the kinds of soft mode and precursor effects described here.

The support of the Australian Research Council, the Australian Partnership for Advanced Computing and the Australian Synchrotron Research Program are gratefully acknowledged. DJG gratefully acknowledges the support of the Australian Institute of Nuclear Science and Engineering. The authors thank Dr Tony Willis of the Research School of Chemistry for assistance with the collection of the Bragg data and Dr Peter Lee of the Advanced Photon Source for assistance with the collection of the diffuse scattering data. Use of the Advanced Photon Source was supported by the US Department of Energy, Office of Science, Office of Basic Energy Sciences, under contract No. DE-AC02-06CH11357.

References

Bar, I. & Bernstein, J. (1977). *Acta Cryst.* B**33**, 1738–1744.
Bar, I. & Bernstein, J. (1982). *Acta Cryst.* B**38**, 121–125.
Beasley, A. G., Welberry, T. R. & Willis, A. C. (2008). *Acta Cryst.* C**64**. In preparation.
Bernstein, J. (2002). *Polymorphism in Molecular Crystals.* IUCr Monographs on Crystallography. Oxford University Press.
Bernstein, J., Bar, I. & Christensen, A. (1976). *Acta Cryst.* B**32**, 1609–1611.
Day, G. M. *et al.* (2005). *Acta Cryst.* B**61**, 511–527.
Day, G. M., Motherwell, W. D. S. & Jones, W. (2007). *Phys. Chem. Chem. Phys.* **9**, 1693–1704.
Estermann, M. A. & Steurer, W. (1998). *Phase Transitions*, **67**, 165–195.
Goossens, D. J., Heerdegen, A. P. & Welberry, T. R. (2008). *Acta Cryst.* B**64**, 456–465.
Kabsch, W. (1993). *J. Appl. Cryst.* **26**, 795–800.
Knapman, K. (2000). *Mod. Drug Discovery*, **3**, 53–54.
Lommerse, J. P. M. *et al.* (2000). *Acta Cryst.* B**56**, 697–714.
Motherwell, W. D. S. *et al.* (2002). *Acta Cryst.* B**58**, 647–661.
Neumann, M. A., Leusen, F. J. J. & Kendrick, J. (2008). *Angew. Chem. Int. Ed.* **47**, 2427–2430.
Proffen, Th. & Welberry, T. R. (1997). *Acta Cryst.* A**53**, 202–216.
Weber, T. & Bürgi, H.-B. (2002). *Acta Cryst.* A**58**, 526–540.
Weber, T., Estermann, M. A. & Bürgi, H.-B. (2001). *Acta Cryst.* B**57**, 579–590.
Welberry, T. R. (2004). *Diffuse X-ray Scattering and Models of Disorder.* IUCr Monographs on Crystallography. Oxford University Press.
Welberry, T. R., Goossens, D. J., Edwards, A. J. & David, W. I. F. (2001). *Acta Cryst.* A**57**, 101–109.
Welberry, T. R., Goossens, D. J., Heerdegen, A. P. & Lee, P. L. (2005). *Z. Kristallogr.* **222**, 1052–1058.
Welberry, T. R. & Heerdegen, A. P. (2003). *Acta Cryst.* B**59**, 760–769.
Welberry, T. R., Proffen, Th. & Bown, M. (1998). *Acta Cryst.* A**54**, 661–674.